

# Building Large Area CZT Imaging Detectors for a Wide-Field Hard X-ray Telescope – *ProtoEXIST1* <sup>★</sup>

J. Hong, B. Allen, J. Grindlay, N. Chammas<sup>1</sup>

*Harvard-Smithsonian Center for Astrophysics, Cambridge, MA 02138*

S. Barthelemy, R. Baker, N. Gehrels

*NASA Goddard Space Flight Center, Greenbelt, MD 20771*

K. E. Nelson, S. Labov, J. Collins<sup>2</sup>

*Lawrence Livermore National Laboratory, Livermore, CA 94550*

W. R. Cook, R. McLean, and F. Harrison

*California Institute of Technology, Pasadena, CA 91125*

## Abstract

We have constructed a moderately large area (32 cm<sup>2</sup>), fine pixel (2.5 mm pixel, 5 mm thick) CZT imaging detector which constitutes the first section of a detector module (256 cm<sup>2</sup>) developed for a balloon-borne wide-field hard X-ray telescope, *ProtoEXIST1*. *ProtoEXIST1* is a prototype for the High Energy Telescope (HET) in the Energetic X-ray imaging Survey Telescope (*EXIST*), a next generation space-borne multi-wavelength telescope. We have constructed a large (nearly gapless) detector plane through a modularization scheme by tiling of a large number of 2 cm × 2 cm CZT crystals. Our innovative packaging method is ideal for many applications such as coded-aperture imaging, where a large, continuous detector plane is desirable for the optimal performance. Currently we have been able to achieve an energy resolution of 3.2 keV (FWHM) at 59.6 keV on average, which is exceptional considering the moderate pixel size and the number of detectors in simultaneous operation. We expect to complete two modules (512 cm<sup>2</sup>) within the next few months as more CZT becomes available. We plan to test the performance of these detectors in a near space environment in a series of high altitude balloon flights, the first of which is scheduled for Fall 2009. These detector modules are the first in a series of progressively more sophisticated detector units and packaging schemes planned for *ProtoEXIST2* & *3*, which will demonstrate the technology required for the advanced CZT imaging detectors (0.6 mm pixel, 4.5 m<sup>2</sup> area) required in *EXIST*/HET.

*Key words:* X-ray Imaging, CZT

## 1. Introduction

The Burst Alert Telescope (BAT), launched aboard *Swift* - a multiwavelength Gamma-ray Burst mission, opened a new era of hard X-ray imaging with the first large array of CZT detectors in space [3]. CZT detectors are ideal for use in high

<sup>★</sup> Send correspondence to J. Hong :

E-mail: jaesub@head.cfa.harvard.edu,

See the electronic edition for the color version of the figures for clarity.

<sup>1</sup> Now at G2 System LLC, Boston, MA 02110

<sup>2</sup> Now at XIA LLC, Hayward, CA 94544

energy astronomy as the high  $Z$  composition stop X-ray photons efficiently, the large band gap allows room temperature operations with excellent spectral resolutions. Arrangement of contacts in pixels or strips on these detectors allow for the precise reconstruction of the positions of incident X-rays. In addition to X-ray astronomy CZT detectors also have a wide range of applications including medical imaging and radiologic interdiction.

For our purposes we intend to utilize this technology in a next generation hard X-ray telescope - the Energy X-ray Imaging Survey Telescope (*EXIST*)<sup>3</sup>. *EXIST* is the leading candidate for the Black Hole Finder Probe under NASA's Beyond Einstein Program<sup>4</sup>, which is currently undergoing further development as part of the Advanced Mission Concept Study Program<sup>5</sup>. The main goals of *EXIST* are to perform an unbiased survey of black holes on all scales and to probe the early universe through the detection of high redshift ( $z \gtrsim 7$ ) GRB's.

The High Energy Telescope (HET) on *EXIST* employs CZT detectors in a coded-aperture imaging telescope, which are similar to the ones in the *Swift*/BAT but significantly advanced. In coded-aperture imaging, the sensitivity of the telescope is proportional to the square root of the detector area. Therefore, a large area of fine pixel CZT detectors is essential, in order to achieve the ambitious science goals of the *EXIST* mission. The construction of such detectors, which can operate using the limited resources available in a space environment (e.g. power), is a key challenge for the *EXIST* mission.

The CZT detectors on the *Swift*/BAT cover about 0.5 m<sup>2</sup> with approximately 31000  $4 \times 4 \times 2$  mm<sup>3</sup> CZT crystals, where each crystal works as an individual pixel element, and are sensitive between 15 and 150 keV. *EXIST*/HET requires a detector plane spanning approximately 4.5 m<sup>2</sup> and a pixel size of 0.6 mm. This is about 10 times the detector area with 7 times finer pixelation than found in BAT; The HET will have about a factor of 400 more pixels (13M). In addition, the HET will cover a wide energy range (5 - 600 keV). The CZT crystals will be 5 mm thick in order to efficiently detect X-rays at energies above 200 keV. In order to achieve the desired 5 keV threshold extremely low noise electronics are also required. The power restrictions for

a space-based mission also require that the power consumption for each channel be extremely low.

These constraints can only be achieved with a very efficient packaging scheme utilizing sophisticated detector and electronics arrays. For *EXIST*, we plan to employ 13000 closely tiled multi-pixel CZT crystals ( $20 \times 20 \times 5$  mm<sup>3</sup>, 1024 pixels), each of which is bonded onto an Application Specific Integrated Circuit (ASIC) that consumes approximately 20  $\mu$ W/pixel.

Currently we are developing the CZT technology required for *EXIST* in a series of balloon experiments dubbed *ProtoEXIST*. In *ProtoEXIST1*, the first in the series, we will construct two large modules ( $2 \times 256$  cm<sup>2</sup>) of tightly packaged CZT detectors with 2.5 mm pixel. In *ProtoEXIST2*, we will refine the backend electronics to allow for detectors with 0.6 mm pixel, and finally in *ProtoEXIST3*, we will assemble a CZT detector module (256 cm<sup>2</sup>) that can be used in *EXIST*.

We have assembled a part ( $8 \times 4$  cm<sup>2</sup>) of the first module for *ProtoEXIST1* which consists of 8 tiled  $2 \times 2$  cm<sup>2</sup> CZT detectors. This module is fully operational and, as we continue to acquire CZT crystals, we expect to complete the two detector modules within the next 3 months in order to assemble two complete coded-aperture telescopes for the first *ProtoEXIST1* balloon flight set for the Fall of 2009.

In this paper we introduce the packaging scheme that enables gap-free tiling of a large number of CZT detectors (§2). We review unique features in the data collected from these CZT detectors (§3) and present the performance for the first *ProtoEXIST1* sub-module using an <sup>241</sup>Am radioactive source (§4). Finally we outline our development plan for the next series of detector modules for *ProtoEXIST2* & 3 (§5).

## 2. Modularization Scheme

Here we review the detector packaging and operation scheme developed for *ProtoEXIST1* (Fig. 1). An extensive description of the early development of the telescope and detector plane can be found in [4,5,6]

### 2.1. Detector Crystal Unit (DCU)

The basic building blocks from which the *ProtoEXIST1* detector plane is constructed are called Detector Crystal Units (DCU). Each DCU consists

<sup>3</sup> <http://exist.gsfc.nasa.gov>

<sup>4</sup> <http://universe.nasa.gov/>

<sup>5</sup> [http://www.nasa.gov/home/hqnews/2008/feb/HQ\\_08054\\_Astro\\_Concept\\_Studies.html](http://www.nasa.gov/home/hqnews/2008/feb/HQ_08054_Astro_Concept_Studies.html)

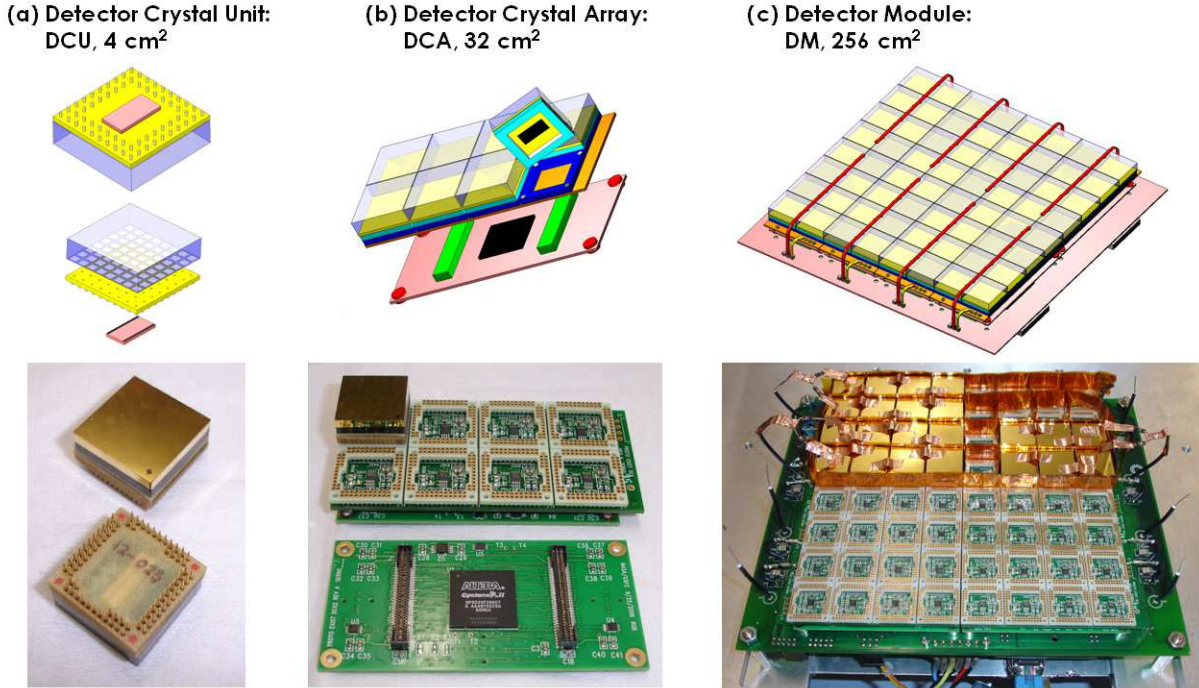


Fig. 1. The modularization scheme for large area CZT imaging detectors. (a) Detector Crystal Unit (DCU): a CZT crystal (blue), an IPB (yellow) and a RadNet ASIC (pink) (b) Detector Crystal Array (DCA): 2x4 DCUs, a DCU Socket board and a DCA FPGA board (c) Detector Module (DM): 2x4 DCAs and an FPGA controller board. In the picture, (a) a red dot on the Au cathode surface of the crystal indicates the orientation of the crystal with respect to the IPB, and the RadNet ASIC is partially visible through the protection cover (see also Fig. 3) (b) one DCU is mounted on the DCA board, (c) 20 DCUs and 8 DCA boards are mounted in the picture, with each DCU surrounded by a shield to reduce the interference between the DCUs. Copper tape is used to apply the HV bias for easy testing, mounting, and unmounting of the DCUs.

of a 5mm thick,  $2 \times 2 \text{ cm}^2$  CZT crystal and an electronic circuit board called the interposer board (IPB) which matches the form factor of the CZT. The interposer contains a single ASIC and is directly bonded to the CZT on the side opposite the ASIC as shown in Fig. 1a.

### 2.1.1. CZT crystal

We utilize CZT crystals obtained from Redlen Technologies<sup>6</sup> which has developed a traveling heater CZT growth technique that enables the production of highly uniform CZT crystals at low cost. Each Redlen crystal comes with gold contacts deposited on both the cathode and anode sides. The anode side has a pattern of  $8 \times 8$  square pixels with a 2.46 mm pitch and a 2.0 mm pad size. These typically exhibit leakage currents of  $\lesssim 0.5 \text{ nA/pixel}$  under a HV bias of -600 V on the cathode. The reversal of the anode and cathode or the polarity

of the HV bias results in leakage currents which are approximately an order of magnitude larger, i.e. there is a preferential orientation for low leakage currents in Redlen CZT crystals.

Before the attachment of a CZT crystal to an IPB a leakage current measurement is performed in order to determine the correct orientation of the cathode and anode. The original Redlen contacts are then stripped from the CZT and replaced in preparation for the IPB bonding process. Next the CZT crystals are then bonded onto the IPB's using a low temperature ( $\sim 100\text{--}120^\circ\text{C}$ ) solder bonding technique, developed at Aguila Technologies<sup>7</sup>, which is significantly less expensive than other bonding techniques that are current available. The solder bonds provide both the mechanical support and electric connection between the 64 anode pixels and the matching input pads on the IPB.

<sup>6</sup> <http://www.redlen.com>

<sup>7</sup> <http://www.aguilatech.com>

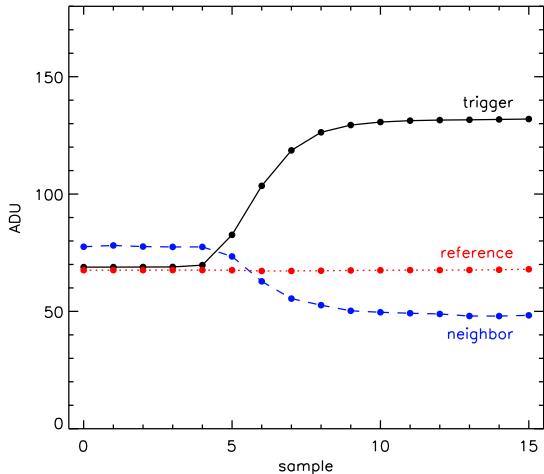


Fig. 2. Example pulse profiles averaged over events. For each event, the RadNet ASIC can record 16 samples of the pulse profile for triggered pixels (solid black), neighboring pixels (dashed blue), and the rest of the pixels unrelated to the event (dotted red).

### 2.1.2. Interposer Board (IPB)

The IPB is an eight layer board which maps the 2-D  $8 \times 8$  array of anode pixels to  $1 \times 64$  input pads of the ASIC affixed to the back side of the IPB. The design of the IPB has been revised a number of times in order to achieve optimal performance. For instance, in order to reduce the capacitance noise on the ASIC input, we introduced narrow traces (3 mil) and the low dielectric constant material (Arlon NT55 or ST55) for the latest revision of these boards. The capacitance-induced noise estimates and the measured electronics noise of the bare DCUs (IPB+ASIC, no crystal) match very well [4,5], demonstrating one of the dominant components of electronics noise we observe is the large capacitance of the long traces in the IPB's between the anode pixels and the ASIC inputs (see also Fig. 11 in §5).

### 2.1.3. RadNet ASIC

To process signals from the *ProtoEXIST1* CZT detectors, we employ the RadNet ASIC. The RadNet ASIC was originally developed for Homeland Security programs [7], and has inherited the circuitry design from an ASIC used for a balloon-borne focusing hard X-ray telescope, HEFT [2]. HEFT was a pathfinder for the upcoming hard X-ray focusing space telescope, NuSTAR<sup>8</sup>, which will employ CZT detectors at the focal plane.

<sup>8</sup> <http://www.nustar.caltech.edu/>

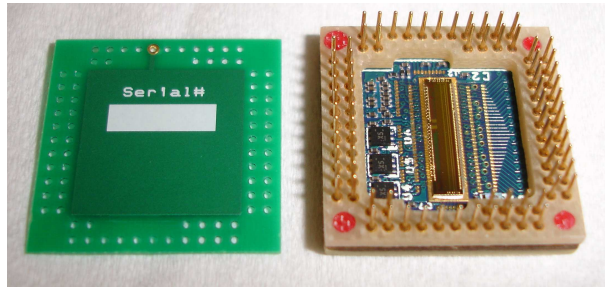


Fig. 3. The bottom DCU shield and the backside of the bare DCU without a CZT crystal. The bottom DCU shield fits on the IPB socket and protects the wire bond of the ASIC and electrically shields the ASIC.

The RadNet ASIC has many features that are particularly attractive for our application. Compared to other known ASICs, one of the main advantages is its relatively low power consumption (less than  $100 \mu\text{W}/\text{pixel}$ ) which is essential for the operation of a large number of channels or pixels as required in *EXIST* which will contain more than 10 M pixels with a total power consumption under about 300 W.

In addition, the RadNet ASIC provides a wide dynamic range (10 keV – 1 MeV) with a low intrinsic electronics noise, which is approximately  $170 e^-$  root mean square (rms) or about 1.5 keV full width half maximum (FWHM). It is also capable of multi-pixel pulse-profile readout, which can provide the depth ( $z$ ) information of the interaction as well as  $x, y$  and the energy deposit ( $E$ ). The flexible readout mode also allows for the complete reconstruction of multi-pixel trigger events arising from charge splitting or Compton scattering [5,9]. The reconstruction of Compton scattered events makes possible the polarization measurement of detected X-rays and the full recovery of the total energy deposited through multiple interactions within the detector. The interaction depth ( $z$ ) is also useful for reducing background even for events with a single triggered pixel arising from photoelectric interactions (e.g. low energy events occurring near the anode side are likely background). It is also important for refining imaging with crystals thicker than the pixel width.

The basic architecture of the RadNet ASIC can be found in the literature [2]; here we briefly review its operation. Every pixel or channel in the ASIC continuously amplifies input signals, which are sampled at a user-selected rate from 2 (normal) to 4 MHz and stored in a bank of 16 capacitors. When a trigger occurs, the ASIC continues to sample and store 8 more values, so that one can extract 8 pre- and post-trigger samples for the event. Fig. 2 shows



example pulse profiles. The signal height is determined by the difference between the average of the first 5 pre-trigger sampling points and the average of the last 7 post-trigger sampling points. Excluding the rising or falling section of the pulse profile and averaging over the maximum number of samples possible for the pre- and post-trigger samples reduces the statistical fluctuation of electronics noise, which could otherwise dominate the uncertainty in the pulse height measurement.

Note that the apparent rise time of the pulse profile (about 2  $\mu$ sec, 4 or 5 samplings at 2 MHz) does not represent the charge drift time ( $< 0.5 \mu$ s) in the CZT crystal under the HV but rather is dominated by charge coupling between the successive sampling capacitors<sup>9</sup>. Therefore, one cannot use the apparent rise time for deriving the depth of the interaction, however there exists an alternative method.

The pulse profile readout scheme makes possible the measurement of negatively induced charges without need for additional circuitry to process signals of the opposite polarity. As shown in the blue profile of Fig. 2, when the post-trigger samples are lower in amplitude than the pre-trigger samples, negatively induced charges are then recorded. Negative charges are usually induced in pixels neighboring triggered pixels due to slow-moving holes, and the total sum of the induced signal in neighbor pixels is proportional to the depth of the interaction [8,5,9].

We have demonstrated this new depth sensing method which takes advantage of negatively induced charges for the first time in a pixellated CZT detector [5]. We have achieved sub-mm depth sensing precision in the 5 mm thick CZT crystal of the first revision (rev1) DCU. In a subsequent paper, we will model in detail this depth sensing procedure and address its prospect for the current version (rev2) and the future revision (0.6mm pixel) of CZT detectors based on electrostatic models and measurements [9].

#### 2.1.4. DCU shields

The initial test runs with the simultaneous operation of multiple DCUs revealed the presence of interference between the DCUs. This interference and the subsequent increase of the electronics noise are more prominent in pixels tied to long traces in the IPB under a HV bias. In order to minimize this we have devised simple electric shields surrounding the

five sides of the IPB in each DCU. The bottom side is covered by a simple electronic board with a single ground plane that is coupled to the ground pin of the DCU through a single trace (Fig. 3). The bottom shield replaces the partially transparent cover (shown in Fig. 1a, the back cover labelled 12-023) that protects the ASIC wirebonds. For the four side walls, we have manually constructed thin shields, which are a thin copper tape sandwiched by Kapton tape for electrical insulation. The side shields cover all side surfaces of the DCU from the top of the cathode to the bottom of the rear shield (Fig. 1c). These shields reduce the noise down to the level observed when operating a single DCU.

#### 2.2. Detector Crystal Array (DCA)

The next largest element in our modularization scheme is the Detector Crystal Array (DCA), which combines  $2 \times 4$  array of DCU's on two vertically-stacked electronics boards (Fig. 1b). The vertical stacking is introduced to package the necessary electronics without introducing any additional footprint so that we can tile crystals with a minimal gap for the construction of a large continuous detector plane.

Mounted on the upper board is a  $2 \times 8$  array of DCU sockets. In the current revision, we only allow a 400  $\mu$ m gap in between 20 mm x 20 mm crystals for easy (un)mounting DCUs and the side shields situated between them. The upper board is about 5 mm longer than the lower board, extending beyond the edge of the DCU sockets on one side. This extension is for direct connection between the HV ground and the ASIC analog ground, so that a series of RC filters for the HV bias can be electrically and physically close to the ASIC for noise reduction. This extension is introduced mainly for convenience in the initial experiment; the immediate connection can be still achieved with very minimal or no extension of the board beyond the detector plane  $16 \times 16 \text{ cm}^2$ .

An Altera<sup>10</sup> Cyclone II FPGA (EP2C20F256C7) is mounted on the lower DCA board to process signals from the DCU's by commanding eight ASIC's and four 16-bit ADC's (AD7685BRM) mounted on the upper board. The signals from the DCU's are processed in pairs, so there are four data streams on a DCA. The DCA FPGA is programmed to have four corresponding channels, each of which controls two DCU's and shares an ADC in parallel in order

<sup>9</sup> This defect is fixed in the new ASIC for *ProtoEXIST2*. See §5.

<sup>10</sup><http://www.altera.com>

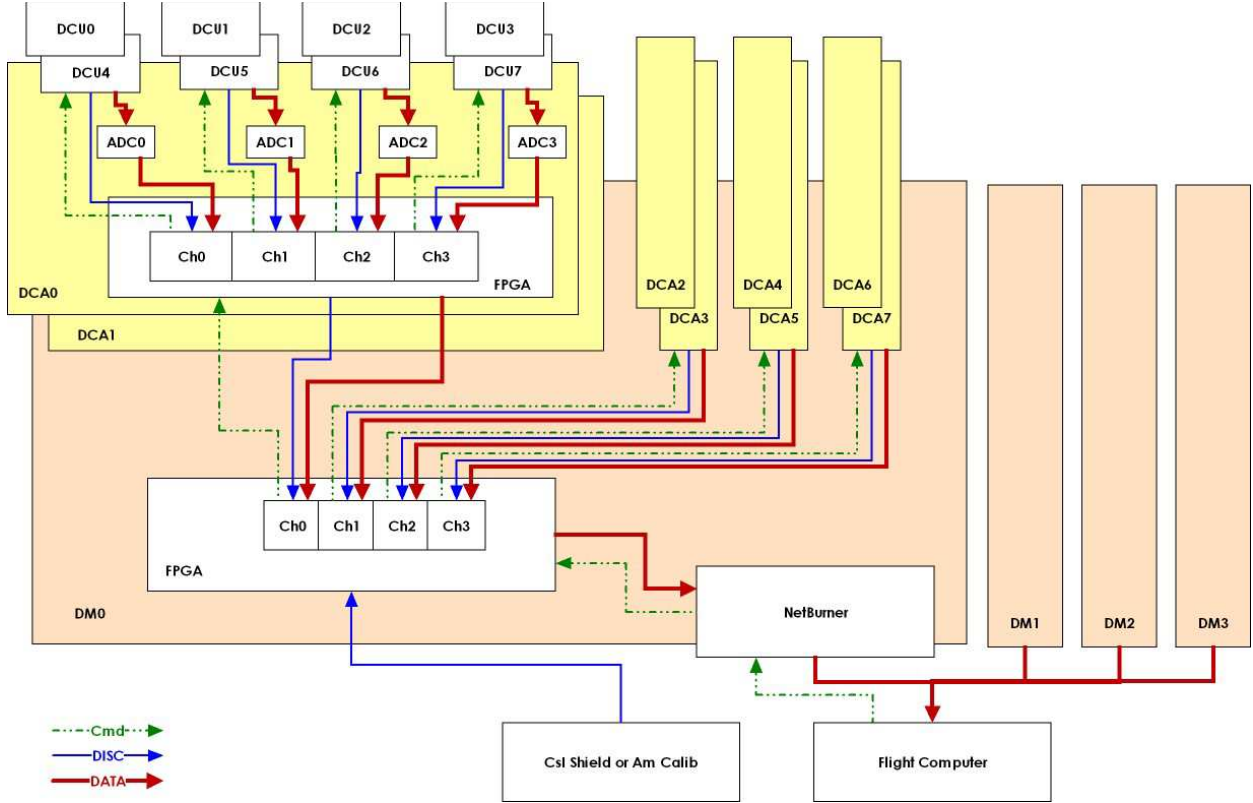


Fig. 4. Schematics of the data stream and signal processing of *ProtoEXIST1*. The DCA FPGA has four independent channels of the data streams and each channel processes signals from two DCUs. Similarly the FCB FPGA has four independent data streams and two DCAs share one stream.

to minimize the dead time caused by the event processing in other pairs.

The signal readout from the RadNet ASIC is highly customizable. For a given event, one can read out the 16 samples of the pulse profile from any number of pixels. All 16 samples of the 64 pixels for an event in a DCU may even be readout for a single event. Such a readout mode provides a complete snapshot of the ASIC for the event at the expense of increased signal processing time. Since a complete snapshot of the DCU is not always necessary, we have implemented multiple readout modes in each of four channels in the DCA FPGA, where one can read out just one designated pixel (Debug Mode), triggered pixels (Fast Mode), triggered + neighboring + reference pixels (Normal Mode), or all 128 pixels of both DCU's in the same pair (Calibration Mode). Table 1 summarizes the readout modes for a DCU pair. The main bottleneck in the event processing pipeline is the ASIC readout which requires about  $30 \mu\text{s}$  for each sample (about 0.5 ms/pixel). This is due in part to the conservative

ASIC readout scheme we have implemented in the DCA FPGA. In principle we can increase the data readout speed from the RadNet ASIC by a factor of 2 over the current implementation, however the current count rate limit is well above the  $1 \text{ cps cm}^{-2}$  that is expected in flight.

Table 1  
Readout mode ( $N$  trigger pixels per DCU pair)

Mode	pixels to read	words /event	dead time /event (msec)	max count rate/DCU pair (cps)
debug	1	39	0.5	700
trigger	$N$	$23+16N$	$0.5 N$	$700/N$
normal	$5 \dots 128$	$103 \dots 2071$	$2.5 \dots 32$	$10 \dots 160$
calibration	128	$55+144N$ 2071	$4.5 N + 1$ 32	$350/(4.5N+1)$ 10

DCU pair:  $8 \text{ cm}^2$

### 2.3. Detector Module (DM)

A Detector Module (DM) for a telescope in *ProtoEXIST1* is composed of a  $2 \times 4$  array of DCA's mounted on a motherboard, called the FPGA controller board (FCB), as shown in Fig. 1c. The FCB contains eight sets of sockets for mounting eight DCAs on the top side. Another type of Altera Cyclone II FPGA (EP2C20F484C7) is mounted on the back side for the control and processing of signals from the DCA's. The DCA mounting sockets on the FCB's are arranged so that the 20.40 mm pitch of the DCU sockets remains constant over the entire DM. Similar to the DCA FPGA, we configured the FCB FPGA to have four independent data channels with each channel reserved to process the data stream from two DCA's as illustrated in Fig. 4.

Two EMCO<sup>11</sup> miniature HV power supplies (PS) are also attached to the FCB in order to bias the cathode surface of 64 crystals normally at  $-600$  V. Each HVPS provides the bias for half of the DCU's present on the FCB. The output from the HVPS is split into 4 separately filtered leads that provide the HV bias for all DCU's on a single DCA. The lead for each DCA provides the bias for 8 individual DCU's whose cathodes are coupled using conductive Copper tape.

During the upcoming balloon flight each detector plane will be surrounded by four passive side shields and a rear active shield. The passive shield is composed of multilayer sheets of Pb/Ta/Sn/Cu, and the active shield is a  $26 \times 26 \times 2$  cm<sup>3</sup> CsI scintillator outfitted with two photo-multipliers (PMTs). For on board calibration of each DM during the flight, we employ a small plastic scintillator doped with <sup>241</sup>Am. For each 59.6 keV X-ray photon generated in the <sup>241</sup>Am, the associated  $\alpha$ -particle triggers the PMT coupled to the scintillator. We will use two <sup>241</sup>Am calibration sources to uniformly irradiate the DM. The trigger signals from these shield and calibration PMTs are fed into the DM through the TTL line for tagging of the shield and calibration source events. For time tagging, 1 pulse per second (PPS) TTL pulse from a Global Positioning Unit (GPS) is fed to the DM. The detail about the CsI shield, the onboard <sup>241</sup>Am radioactive sources and the GPS driven clock will be given in [1].

When a trigger occurs, the fast trigger signal ( $< 0.5$   $\mu$ sec) alerts the corresponding channel of both

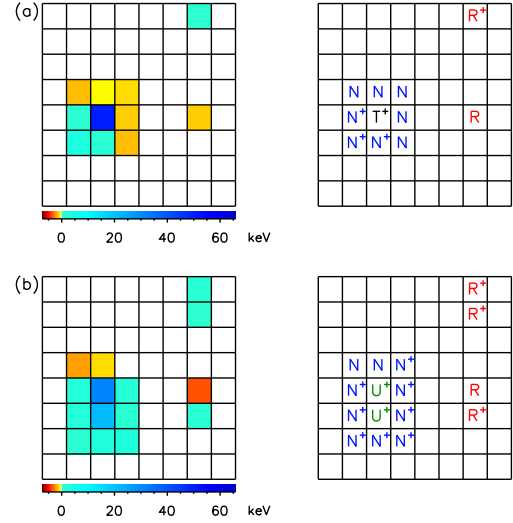


Fig. 5. Example events in a DCU; the top two panels show the calibrated signals and the pixels marked for readout from a single pixel trigger event, and the bottom two panels show the same for a two pixel trigger event. The (black) 'T's are for isolated trigger pixels, the (green) 'U's for unisolated trigger pixels, the (blue) 'N's for neighbor pixels, and the (red) 'R's for reference pixels. The '+'s indicate positive energy deposits.

the DCA FPGA and the FCB FPGA. While the DCA FPGA starts the data readout sequence from the ASIC, the FCB FPGA checks the shield signals, the <sup>241</sup>Am calibration source status, and the clock counter and then insert them into the data stream when the DCA FPGA passes the data to the FCB FPGA.

### 2.4. Flight Computer and Data Collection

The DM communicates with the flight computer through ethernet via a Netburner card<sup>12</sup> mounted on the backside of the FCB for the transfer of data and command and control. The Netburner card collects data from the four data channels of the FCB FPGA and the housekeeping (HK) data of the FCB and passes them on to the flight computer. The HK data includes the event trigger rates, the <sup>241</sup>Am calibration source rate, the CsI rear shield count rates, input voltages and currents of the low voltage PS units, temperature and pressure of the vessel, etc. The Netburner card also controls the HV setting and passes the commands for the ASICs such as the threshold setting for each DCU. Note all 64 pixels in each DCU share a common threshold.

<sup>11</sup><http://www.emcohighvoltages.com>

<sup>12</sup><http://www.netburner.com/>

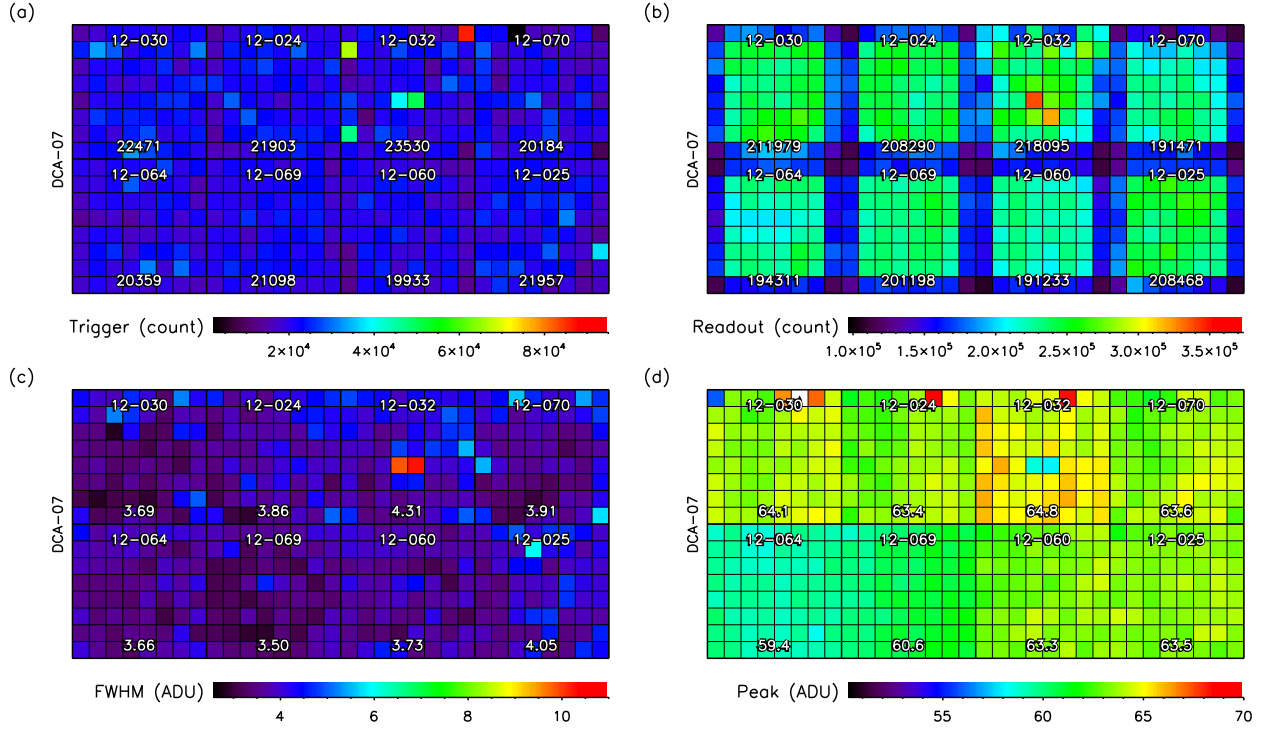


Fig. 6. Raw data taken from an  $^{241}\text{Am}$  source: (a) the trigger count map, (b) the readout count map, (c) the energy resolution (FWHM in ADU) at 59.6 keV, and (d) the peak position (in ADU) of the pulse height histogram for 59.6 keV X-rays. 1 keV is roughly 1.05 ADU.

### 3. Data Analysis

As time of this writing, we have 22 working DCUs. Here we present the analysis results of the data taken with the first eight DCUs using a  $^{241}\text{Am}$  radioactive source shining on the cathode side of the detectors.

The data were taken in the normal readout mode, which reads out all triggered pixels plus all pixels adjacent to triggered pixels on the same DCU and 2 unrelated reference pixels for zero point calibration. Fig. 5 shows an example of the charge deposit map and the readout pixels for an event with an isolated trigger pixel (a total of 11 pixels to be read out) and the same for a charge split event with two trigger pixels (16 pixels to be read out). In principle, one can read out the signals from the neighbor pixels in the neighbor crystals when a trigger occurs on edge or corner pixels, but for now we limit the neighbor pixel readout within one DCU because the side DCU shield prevents the neighbor crystal from inducing negative charges.

Due to the complexity and the unique nature of the data provided by the *ProtoEXIST1* CZT detectors, it is worthwhile to explore the properties of the

raw data and the calibration procedure for future reference.

#### 3.1. Raw Data and Calibration

Fig. 6 shows pixel map views of the raw  $^{241}\text{Am}$  data: (a) the total trigger count, (b) the readout count map, (c) the energy resolution (FWHM) and (d) the peak position of the pulse height histogram for the 59.6 keV X-rays from the source. Each crystal is labelled by the DCU ID (e.g. 12-030) and the pixel-averaged quantity of the display (e.g. 22471 trigger counts for 12-030). The raw pulse height is given in our custom unit - ADU, where 1.05 ADU is approximately 1.0 keV.

The trigger count map shows there are a few hot pixels. The readout map appears as a tiled pattern of squares which is due to the dearth of neighboring pixels on the edges, which when triggered would otherwise initiate a read sequence. The energy resolution ( $2.23\sigma$ ) and the peak values ( $E_p$ ) are derived from a gaussian fit with no constant term ( $A_0 \exp[-(E - E_p)^2/4/\sigma^2]$ ) to the pulse height histogram of each pixel.



As previously mentioned, the pulse height is calculated by subtracting the average of the first 5 pre-trigger samples from the average of last 7 post-trigger samplings. A trigger can occur during samples by any one of the 16 capacitors and small variations in the capacitance values of the 16 capacitors may cause the resulting pulse height to vary depending on the triggering capacitor ID (CapID). Therefore a CapID dependent calibration must be applied in order to properly convert the raw ADU values into energies. Fig. 7a shows the CapID dependence of the pulse height in the DCU stacked data. The pulse height ( $x$ -axis) is given in the relative ADU from the pulse peak position. This dependence also varies from pixel to pixel (Fig. 7c), so that for calibration, the pulse peak of each pixel for each CapID has to be derived. The right panels in the Fig. 7 show the result after calibration which has removed the pixel- and CapID-driven variation.

### 3.2. Calibrated Data

Fig. 8 shows the energy resolution (FWHM) and the photo peak count map (counts in 50–70 keV) for the calibrated data of the isolated triggered pixels. The figure also shows the pixel distributions of the energy resolution (FWHM) and the photo peak count. The average FWHM is 3.2 keV.

The two pixels in the DCU 12-032 still show a relatively large FWHM ( $\sim 10$  keV) even after the calibration, and we suspect cross talk between the two pixels is caused by a malformed bond due to their physical proximity. Additionally the electric pulser data before bonding the crystal did not show any unusual behavior in these two pixels.

The photo-peak count map or its pixel distribution shows a noticeable variation ( $\sim 20\%$  variation for 68% of the pixels) of measured counts across all pixels despite the relatively uniform irradiation of the DCUs. Note we expect about 1% variations from the statistical fluctuation under the assumption of a Poisson distribution and the measured number of counts. This large variation could be partially the result of high count rates on the DCU's, which were about a factor of 3 higher than the maximum rate the current readout mode can handle without any event loss. Further investigation is required to identify the cause of this large variation. We also plan to measure the absolute quantum efficiency of the CZT detectors using the on board  $^{241}\text{Am}$  calibration sources, which allows the measurement of the

absolute number of X-ray photons emitted by the source as well as the number of captured X-rays in the CZT detectors.

## 4. Results

Fig. 9a shows the calibrated energy histogram of all 8 DCUs (red) in comparison with the raw pulse height histogram (black). For these histograms, we are using the data from isolated triggered pixels ('T's in Fig. 5, see below). The calibrated histograms show an energy resolution of 3.2 keV (FWHM) at 59.6 keV and the two escape peaks around 33 and 37 keV (the red line in the inset in Fig. 9) are well resolved.

Fig. 9b compares the calibrated energy histograms of four different cases of charge collection in pixels: isolated triggered pixels with no triggered neighbors (black 'T's), untriggered neighbor pixels (blue 'N's), untriggered reference pixels (red 'R's), and unisolated triggered pixels with triggered neighbors (green 'U's). Fig. 9b and the right panels in the Fig. 5 use the same color or code scheme for easy comparison. All four histograms show a mild pile-up at 60, 100, and 120 keV respectively.

The isolated triggered pixels (black in Fig. 9b) manifest themselves in events where all or most of the energy deposited from the interaction is confined to a single pixel and the induced charges in neighbor pixels are below the trigger threshold. The histogram falls off just below the 30 keV due to the threshold set around 25 to 30 keV. A peak around  $E = 0$  keV in the histogram is due to a few hot pixels, which can be also spotted in Fig. 7d (e.g. DCU 12-032). These hot pixels are suspected to be due to the unusually high capacitance value in one of 16 sampling capacitors in the ASIC and a relatively high base line for the pixel in question. Since there is no real induced signal in these pixels, the resulting pulse height is centered around zero.

The pulse height histogram of the untriggered neighboring pixels shows a large shoulder on the both sides of the peak at 0 keV (blue in Fig. 9b). The negative side is due to the negative charges induced by slow-moving holes and the positive side is dominated by the charge split from the triggered pixels, where the energy deposited in the untriggered pixel does not exceed the threshold. The histogram for the reference pixels (red in Fig. 9b) is relatively symmetric with respect to 0 keV and does not have large shoulders as expected since no energy is deposited into these pixels or their neighbors. Note the

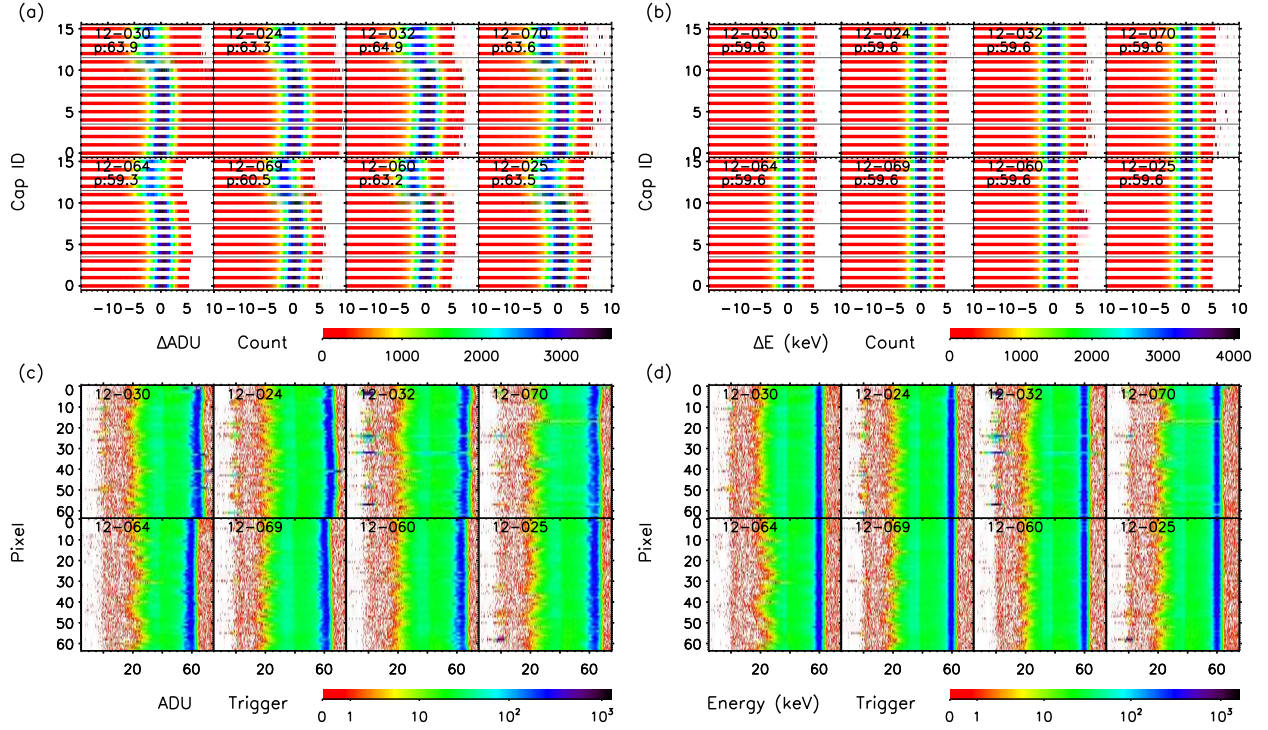


Fig. 7. The CapID and pixel dependence of the pulse height: (a) and (b) CapID vs. the pulse height relative to the peak position, (c) and (d) pixel ID vs. the pulse height. (a) and (c) are in the raw pulse height (ADU), and (b) and (d) are in the calibrated energy (keV).

signal of a reference pixel is used for calibrating the deposited charge of the same pixel in other events, but not for the other trigger or neighbor pixels of the same event.

The energy histogram of the unisolated triggered pixels (green in Fig. 9b) shows a peak around 30 keV, which is due to the fact that it is about half of the energy of the 59.6 keV X-ray photons from the source and the threshold is set around the same 30 keV. For instance, if the charge splits into two pixels with 20 and 40 keV each, only the energy deposit of 40 keV will generate an isolated trigger and the 20 keV deposit will be readout in the untriggered neighbor pixels. On the other hand, if the charge splits into 30 and 30 keV each, both pixels will likely trigger resulting in an unisolated trigger (e.g. Fig. 5b).

The energy histogram of the unisolated triggered pixel indicates some events can trigger a pixel with an induced signal below threshold or even with a negative signal. This is usually due to high energy X-ray events or charged particle (mostly muons) induced events initiating a large electron cloud. In these events, soon after the interaction, the large electron cloud causes multiple pixels to induce positive charges large enough to trigger simultaneously.

As the electron cloud drifts toward a few anode pixels immediately underneath the origin of the cloud, the induced charges in the neighbor pixels begin to be dominated by the slow-moving holes, and as a result, these neighboring pixels can record a sub-threshold signal or even negative signals with their own trigger. Fig. 10 shows the energy deposit and the trigger pixels of such events. A more detailed analysis will be shown elsewhere [9].

## 5. Discussion

Table 2 summarizes the electronics noise and the energy resolution of the *ProtoEXIST1* CZT detectors and the estimated projections for future CZT detectors for *ProtoEXIST2* & 3 and *EXIST*. The performance of the rev1 CZT detectors is taken from the measurement of one good rev1 DCU (01-050) among several DCUs we have produced [5]. For the rev2 CZT detectors, we use the results of the 8 DCUs shown in the previous section. The italicized numbers are the estimated values, based on simple projections based on comparison of the results from <sup>241</sup>Am tests.

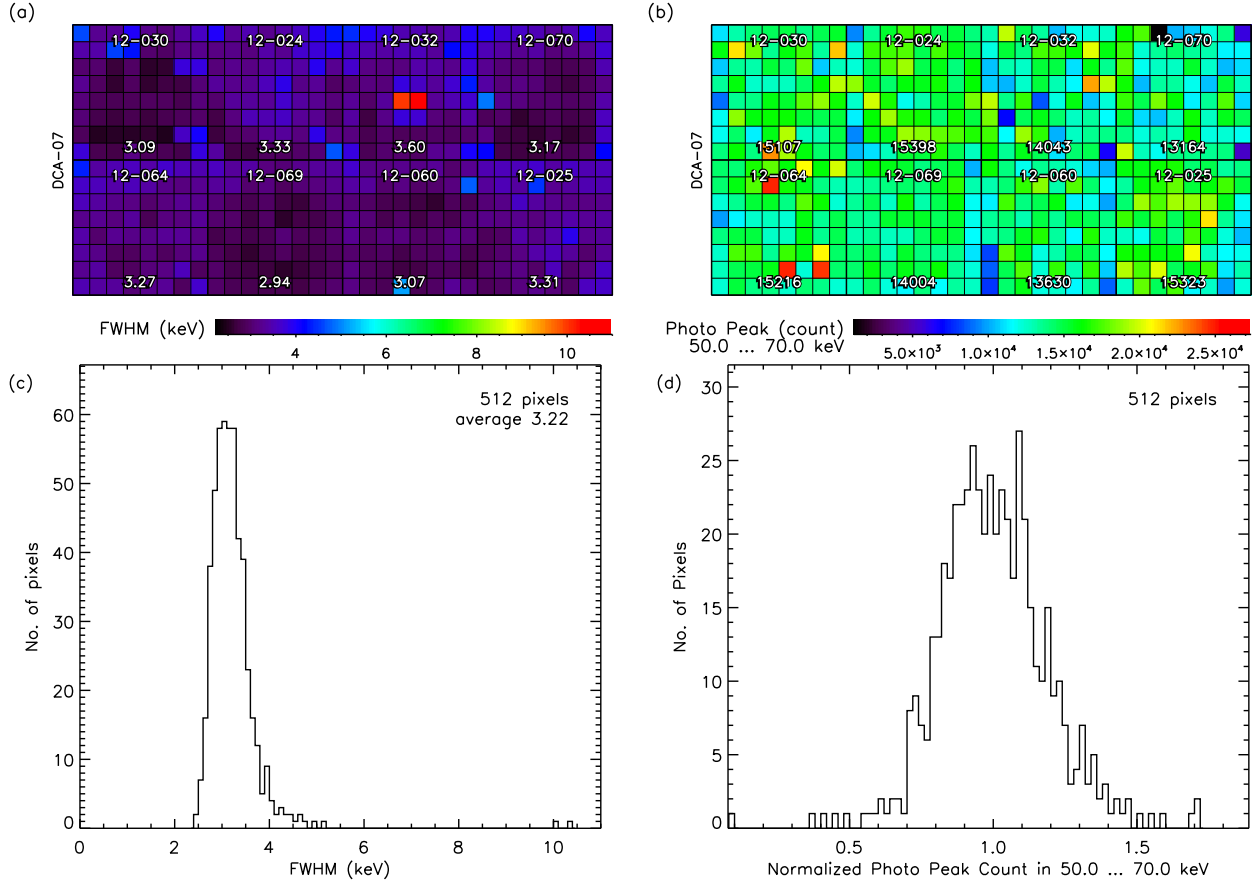


Fig. 8. Calibrated data: (a) the energy resolution map (FWHM), (b) photo-peak count map (50–70 keV), (c) the pixel distribution of the energy resolution, and (d) the same of photo-peak counts.

For the rev2 CZT detectors, we have a 60–70% yield for bare DCUs (ASIC + IPB) with all 64 working pixels and 2.1–2.5 keV FWHM average electronics noise; the 30–40% loss is due to faulty ASIC’s. After bonding the carefully selected and processed CZT crystals to the bare DCU’s, we have a 90% yield for completed DCU’s with the 3.1–3.5 keV FWHM at 60 keV. This is a drastic improvement in yield over the rev1 DCU’s. For *ProtoEXIST1* CZT detectors, we have achieved our goal for energy resolution ( $\lesssim 3.5$  keV FWHM at 59.6 keV) with relatively high yield. The current energy resolution implies  $<1\%$  energy resolution (FWHM) at 662 keV.

CZT imaging detectors in *EXIST* will require 0.6 mm pixels in order to achieve high angular resolution. This high pixel density will be applied for the *ProtoEXIST2* & *3* CZT detectors. In the *ProtoEXIST2* CZT detectors, we will make use of an existing ASIC called the DB ASIC with 1024 channels. The DB ASIC has been developed for the NuSTAR

project, and it inherits and advances the circuitry design from the HEFT ASIC and RadNet ASIC. In the DB ASIC the variations in capacitance values of the 16 sampling capacitors and the coupling between subsequent capacitors have been substantially reduced. This improvement allows for a very low threshold ( $< 5$  keV) and the true representation of the charge drift time in the pulse profile, and may even eliminate the necessity of the CapID-driven calibration. In addition, the DB ASIC also includes the on-chip ADC, which simplifies the back-end electronics and minimize the possible interference among the units.

In NuSTAR, the DB ASIC is directly bonded to the CZT crystal, eliminating the need for an IPB, which is where the designation DB (i.e. direct bond) originates from. The ASIC input form factor matches a CZT crystal with  $32 \times 32$  arrays of anode pixel of 0.6 mm pitch. The matching form factor is also of practical necessity due to the large number of pixels

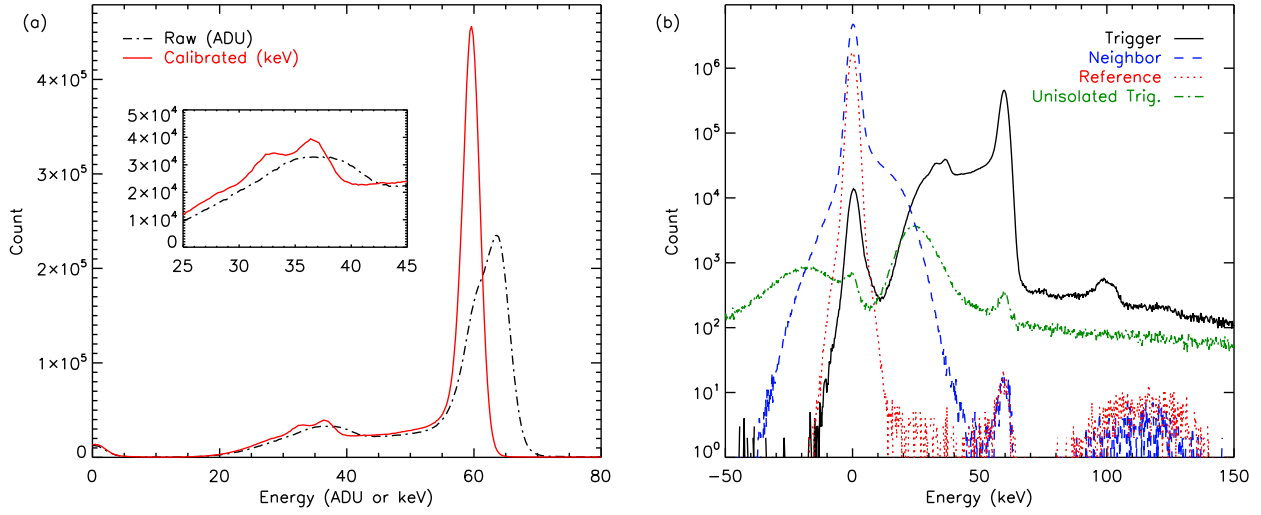


Fig. 9. The energy histogram: (a) the pulse height histogram of the raw data (dashed-dot black) and the calibrated energy histogram (solid red) from the 8 DCUs, and (b) the calibrated energy histograms of four types of charge collection in pixels. The calibrated histogram in (a) shows 3.2 keV FWHM at 59.6 keV and two well resolved escape peaks (the inset). The energy histograms in (b) show charge collection for the isolated triggered pixels (solid black), non-triggering neighbor pixels (dashed blue), non-triggering reference pixels (dotted red), and unisolated trigger pixels (dashed-dot green).

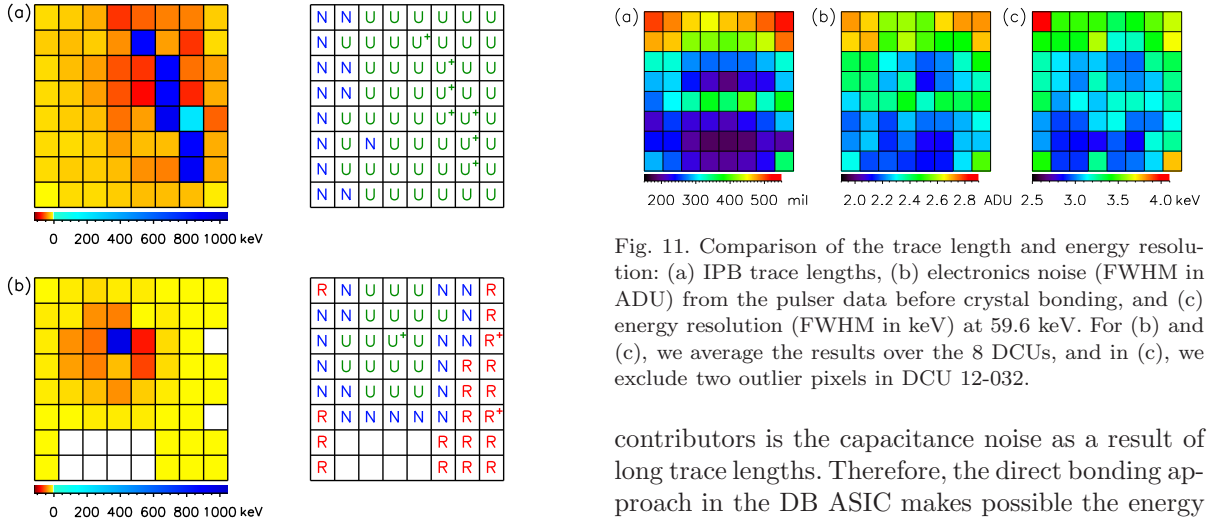


Fig. 10. Example events triggered by muons in a DCU; the top panels show an event with muon coming at an angle and the bottom panels show a case of near normal incidence. The symbols in the right panels are the same as in Fig. 5.

(1024).

Fig. 11 compares the trace lengths in the current rev2 IPB (a) with the electronics noise from the pulser data before crystal bonding (b) and the energy resolution at 59.6 keV for the 8 DCUs used in §3 (c). The electronics noises and the energy resolutions are averaged over the 8 DCUs to reveal the pixel pattern more clearly. The similarity of the patterns in the pixel map indicates one of the main noise

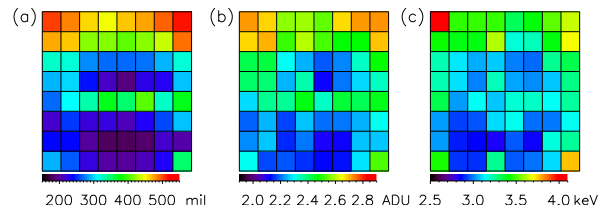


Fig. 11. Comparison of the trace length and energy resolution: (a) IPB trace lengths, (b) electronics noise (FWHM in ADU) from the pulser data before crystal bonding, and (c) energy resolution (FWHM in keV) at 59.6 keV. For (b) and (c), we average the results over the 8 DCUs, and in (c), we exclude two outlier pixels in DCU 12-032.

contributors is the capacitance noise as a result of long trace lengths. Therefore, the direct bonding approach in the DB ASIC makes possible the energy resolution of less than 2 keV by removing the IPB (and the long traces in the IPB). An additional advantage will be the low leakage current for a single pixel which will be about a factor of 16 lower than in *ProtoEXIST1* due to the smaller (0.6 mm) pixel size.

In the *ProtoEXIST2* CZT detectors, we will employ this DB ASIC and apply a packaging scheme similar to that employed in *ProtoEXIST1*. We plan to assemble one DM with 256 cm<sup>2</sup> of the active area for *ProtoEXIST2*, in order to demonstrate the feasibility of signal processing in a large array of the high pixel density CZT detectors.

Fig. 12 shows our packaging scheme for the DCU



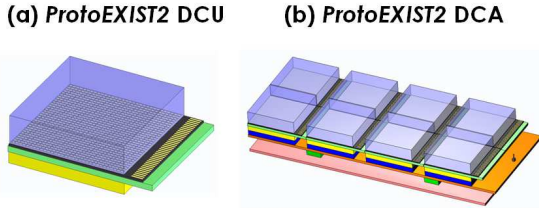


Fig. 12. Modularization scheme for *ProtoEXIST2* CZT detectors.

and DCA of the *ProtoEXIST2* CZT detectors. In *ProtoEXIST2* the CZT crystal is directly bonded to the ASIC, which sits on a small circuit board. Since the DB ASIC requires about 3 mm of space in one direction for control and power lines in addition to the 1024 input pads, we need to allow for a 5 mm gap between DCU's in order to accommodate wirebonds on one side. The DCA board design will likely be simplified due to the inclusion of an ADC in the DB ASIC. The energy resolution estimates in the last column of Table 2 are based on the initial measurement of the CZT detector unit with the DB ASIC [10].

For efficient packaging of a large CZT detector for *EXIST*, we need to minimize the gap between detectors. In addition, the power consumption of the DB ASIC is currently about  $100 \mu\text{W}/\text{pixel}$  which is about a factor five higher than the required value for *EXIST*. Therefore for *ProtoEXIST3* we plan to modify the DB ASIC producing a lower power version, the 'EX' ASIC, to meet these requirements. For gapless packaging we are currently considering two possible options. One method is designed to take advantage of micro-via technology, which would allow the control lines to be brought out to the backside of the chip, such that one could match the footprint of the ASIC and the CZT crystal. In an alternative approach we would either re-package the ASIC in a smaller form factor ( $1.5 \times 1.5 \text{ cm}^2$ ) or use slightly bigger CZT crystals (e.g.  $2.5 \times 2.5 \text{ cm}^2$  with 0.78 mm pixel) and use an interposer board with de-magnifying traces of minimal lengths ( $< 2 \text{ mm}$ ), which map out  $32 \times 32$  anode pixels to  $32 \times 32$  ASIC input pads. We also plan to assemble one DM with a total active area of  $256 \text{ cm}^2$  for *ProtoEXIST3*, which will definitively demonstrate the technologies necessary for the HET on *EXIST*.

## 6. Summary

A large contiguous array of CZT detectors has many applications in hard X-ray imaging. We have demonstrated our innovative packaging scheme for the construction of large CZT detector planes with relatively small pixels. The current working module ( $32 \text{ cm}^2$  with 2.5 mm pixel) shows about 3.2 keV energy resolution at 59.6 keV and we expect to complete two modules ( $512 \text{ cm}^2$ ) as we acquire more CZT crystals. Our packaging scheme will be progressively expanded to demonstrate advanced CZT detectors required for the HET on *EXIST* ( $4.5 \text{ m}^2$ , 0.6 mm pixel size, 5-600 keV).

This work is supported in part by NASA APRA grant NNG06WC12G. Portions of this work were performed under the auspices of the U.S. Department of Energy by Lawrence Livermore National Laboratory under Contract DE-AC52-07NA27344.

## References

- [1] Allen, B., et al., 2009 in preparation.
- [2] Cook, W. R., Burnham, J. A. & Harrison, F. A., 1998 Proc. SPIE, 3445, 347.
- [3] Gehrels, N., et al, 2004 ApJ, 611, 1005.
- [4] Hong, J., et al, 2005 Proc. SPIE, 5898, p173
- [5] Hong, J., et al, 2006 Proc. SPIE, 6219, 63190S
- [6] Hong, J., et al, 2007 Proc. SPIE, 6706, 67060B
- [7] Craig, W. W., Fabris, J. Collins & Labov, S. UCRL-TR-215280
- [8] Eskin, J. D., Barrett, H. H., & Barber, H. B., 1999 J. Appl. Phys. 85, 647
- [9] Hong, J., et al, 2008 in preparation
- [10] Cook, W. R. & McLean, R., Private communication

Table 2

The electronics noise and energy resolution of *ProtoEXIST* CZT detectors (FWHM)

Stage	<i>ProtoEXIST1</i>		<i>ProtoEXIST1</i>		<i>ProtoEXIST2, 3</i>	
	rev1		rev2		& <i>EXIST</i>	
	(keV)	(%)	(keV)	(%)	(keV)	(%)
ASIC intrinsic					0.8 <sup>a</sup>	
After mounting on the IPB	3.1 ± 0.5		2.1 ± 0.3			
After crystal bonding	3.7 ± 0.4		2.5 ± 0.2		1.8 <sup>a</sup>	
under HV (-600V)	4.6 ± 0.6		3.0 ± 0.5		2.0 <sup>a</sup>	
60 keV ( <sup>241</sup> Am)	4.4 ± 1.3	7.3%	3.2 ± 0.5	5.3%	2.2 <sup>a</sup>	3.7%
122 keV ( <sup>57</sup> Co)	5.2 ± 1.4	4.3%	<i>3.8</i>	<i>3.1%</i>	<i>2.6</i>	<i>3.0%</i>
356 keV ( <sup>133</sup> Ba)	7.3 ± 1.9	2.0%	<i>5.3</i>	<i>1.5%</i>	<i>3.7</i>	<i>1.0%</i>
665 keV ( <sup>137</sup> Cs)	7.9 ± 2.5	1.2%	<i>5.7</i>	<i>0.9%</i>	<i>3.9</i>	<i>0.6%</i>

The italicized numbers are the estimates based on the measurements. The measurements show the average electronics noise or energy resolution (FWHM) of the pixels and the  $1\sigma$  distribution. The electronics noise is measured by the internally generated pulses in the ASICs and the true electronics noise is estimated to be slightly smaller than shown here due to intrinsic variations associated with the internal pulses. (e.g. the average FWHM of the electronics noise under the HV (4.6 keV) is smaller than the average FWHM of the energy histogram at 60 keV (4.4 keV) in the rev1 *ProtoEXIST1* CZT detectors). (a) The preliminary results by [10].